Hindawi
International Journal of Energy Research
Volume 2024, Article ID 5572793, 13 pages
https://doi.org/10.1155/2024/5572793

Research Article

Copper Oxide Nanoparticles Anchored on Porous Carbon Nitride Nanosheets for Supercapacitor Applications

Dhananjaya Merum,[1] **Rosaiah Pitcheri**,[1,2] **Nipa Roy**,[1] **Naveen Kumar Kilari**,[3] **Ammar Mohamed Tighezza**,[4] **Soumyendu Roy**,[5] **and Sang Woo Joo**[1]

[1]*School of General Education/Chunma College of General Studies & Department of Physics & School of Mechanical Engineering, Yeungnam University, Gyeongsan 38541, Republic of Korea*
[2]*Department of Physics, Saveetha School of Engineering, Saveetha Institute of Medical and Technical Sciences (SIMATS), Thandalam, Chennai 602105, India*
[3]*Department of Physics, Nitte Meenakshi Institute of Technology, Yelahanka, Bengaluru 560064, India*
[4]*Department of Chemistry, College of Science, King Saud University, P.O. Box 2455, Riyadh 11451, Saudi Arabia*
[5]*Department of Physics and Centre of Excellence in Nanosensors and Nanomedicine, School of Engineering and Applied Sciences, Bennett University, Greater Noida 201310, India*

Correspondence should be addressed to Sang Woo Joo; swjoo@yu.ac.kr

Received 5 July 2023; Revised 12 December 2023; Accepted 9 April 2024; Published 2 May 2024

Academic Editor: Gianluca Coccia

Electrochemical energy storage devices are vital for renewable energy integration and the deployment of electric vehicles. Ongoing research seeks to create new materials with innovative morphologies capable of delivering high specific capacitance for the next generation of customizable energy devices. Carbon nitride is an excellent candidate for electrochemical energy storage devices; however, it has limitations such as layer stacking, poor electric conductivity, a restricted number of electroactive sites, and static electrochemical reaction rates. This research objective is to make porous structures in carbon nitride nanosheets and integrate them with CuO particles to increase surface area and improve electrochemical performance. The use of thermal heating, acidic treatment, and hydrothermal processes accomplishes this. Along with X-ray diffraction peaks of the CuO phase, a prominent peak (002) at 27.67° indicates the presence of graphitic-structured carbon nitride. TEM images show that CuO particles are evenly attached to the surface of g-C_3N_4 nanosheets with lattice intervals of 0.336 and 0.232 nm, which are the (002) and (111) orientations of the g-C_3N_4 and CuO phases, respectively. Adding CuO nanoparticles to porous g-C_3N_4 nanosheets avoids layer stacking and provides micro- and mesopore channels, increasing the specific surface area (42.60 $m^2\,g^{-1}$). The CuO@ porous g-C_3N_4 electrode delivered 817 $F\,g^{-1}$ of specific capacitance at 1 $A\,g^{-1}$ and admirable capacitance retention (92.3% after 6000 cycles) due to the synergistic impact of its unique composition and structural characteristics. Because of its outstanding electrochemical performance and fascinating discoveries, CuO@ porous g-C_3N_4 may be employed as a cathode material for high-performance supercapacitors.

1. Introduction

Pollution-free, renewable energy storage technologies with substantial energy and power densities are essential for advancing civilization and globalization because of the energy crisis in conventional fuels such as coal, oil, and natural gas, as well as those creating environmental degradation and global warming, which severely impact seasons and living species [1, 2]. As a result, researchers have been concentrating on electrochemical energy storage devices that are unaffected by the seasons and climate. Supercapacitors are appealing options for energy storage systems due to their fast charge-discharge features, high power density, ecological friendliness, and cheap cost [3–5]. However, its performance is primarily affected by the electrode's morphological and electrochemical features. As potential supercapacitor

materials, carbonaceous materials, conducting polymers, transition metal oxides, MXenes, metal hydroxides, and sulfides are being investigated. Despite the fact that particle size reduction provides remarkable physiochemical properties, it will be used in a variety of applications in the electrical, medical, and military sectors [6–9]. On the other hand, nanoparticles have an immense specific surface area, enabling them to transport and retain more ions.

Two-dimensional (2D) layered structures have a larger surface area, increasing the number of electrochemically active sites and enhancing reaction kinetics. It also has a low effective mass, which promotes mobility and reduces the bulkiness of any gadget produced from these materials [10, 11]. In this regard, the scientific community is interested in polymeric two-dimensional graphitic carbon nitride (g-C_3N_4) semiconductors due to their exceptional thermal stability, electronic structure, high nitrogen content, organic degradation, photocatalysis, water degradation, nontoxicity, and long-term cycling stability in supercapacitors. The g-C_3N_4 is made up of p-conjugated graphitic orientations formed by the sp2 hybridization of carbon and nitrogen atoms. Unfortunately, the existence of Van der Waal forces between these 2D structures results in laminated sheets with critical issues such as lower conductivity, restricted interlayer spacing, which degrades mass, and ion transport, resulting in reduced active material utilization and poor rate performance [12–15]. Recently, several engineering approaches have been used to adjust structural and compositional tailoring tactics in order to increase electrochemical performance. For example, Ma et al. used in situ oxidative polymerization tracked by direct reduction of Ag^+ to silver particles decorated on PANI/g-C_3N_4 composite and reduced g-C_3N_4 stacking, resulting in an Ag/PANI/g-C_3N_4 electrode with 797.8 F g^{-1} specific capacitance and 84.43% retention after 1000 cycles [16]. Kavil et al. developed metal oxide (CuO, Co_3O_4)-distributed graphitic carbon nitride composites by direct precipitation. The obtained g-C_3N_4/Co_3O_4 electrode has a higher specific capacitance (201 F g^{-1}) than the g-C_3N_4 electrode (72 F g^{-1}) [17]. Similarly, Nabi et al. developed a TiS_2/g-C_3N_4 composite via hydrothermal synthesis by inserting TiS_2 into g-C_3N_4 and suppressing stack layer aggregation. It has strong electrochemical capabilities owing to its reduced charge transfer resistance and enhanced stability over long cycles [18]. Ragupathi et al. employed sol-gel synthesis to investigate manganese sulfide-doped g-C_3N_4 composites. The presence of spherical morphology and a lone pair of electrons in the composite boosts the electrode's conductivity and electrochemical activity [19]. Kong et al. produced a hierarchically porous structured boron-doped g-C_3N_4 electrode material in the form of foam by combining the pore-templating impact of ionic liquids with the contraction effect imparted by a thin carbon-layer covering. The produced B-g-CN_{800} electrode with a large specific surface area (799.6 m^2/g) displayed 660.6 F/g of specific capacitance with excellent cycle stability [20]. According to the literature, the composite of nanoparticles with 2D structures exhibits charming properties due to the synergistic effect of reducing the stacking layer and accelerating the charge transport, as well as improving conductivity, resulting in higher energy and power densities [10]. This revolutionary work provides new impetus for the fabrication of electrode materials for supercapacitors.

Furthermore, another key aspect influencing electrode performance in energy storage is porosity structure, which has significant effects on the specific surface area, electronic conductivity, and electroactive sites. Based on the literature research, carbon nitride nanosheets were produced in this work by heating melamine to 550°C and then employing acid treatment to create porous structures. Finally, metallic oxide (CuO) particles have adhered to the surface of porous carbon nitride nanosheets using a simple one-step hydrothermal technique. The significance of this investigation is the creation of porous structures and the decrease of stacking layers, which offer a high specific surface area. To the best of the authors' knowledge, no prior study on the fabrication of CuO nanoparticles anchored on porous g-C_3N_4 (p-g-C_3N_4) nanosheet electrode materials has been described. In particular, the CuO@ porous g-C_3N_4 (CuO@p-g-C_3N_4) composite has a larger surface area, porous architecture, and better crystallinity than porous g-C_3N_4. Because of the following benefits, these structures are especially well suited for the design of high-energy storage systems: (i) increasing the area of contact between the electrode and electrolyte; (ii) boosting the number of lone pair electrons, which makes more electroactive transmission channels and improves the electrical conductivity of the composite electrode; and (iii) incorporating CuO particles to the surface of the nanosheets, which increases the surface area, electronic conductivity, and faradaic reaction mechanism. The present study is unique in that it uses acidic treatment to create porous g-C_3N_4 and simple hydrothermal synthesis to attach CuO nanoparticles to the surfaces of sheets. The prepared CuO@p-g-C_3N_4 nanosheets are employed as electrodes for electrochemical properties. It outperforms the other reported electrodes in a three-electrode system in terms of specific capacitance, rate capability, and cyclic stability.

2. Experimental Section

2.1. Chemicals. Melamine ($C_3H_6N_6$), hydrochloric acid (HCl), copper chloride dehydrate ($CuCl_2.2H_2O$; 99.99%), polyvinylidene fluoride (PVDF), nitric acid (HNO_3), carbon black, 1-methyl-2-pyrrolidone, polyvinyl alcohol, nickel foam, and potassium hydroxide (KOH; ≥85%) are the ingredients of this work. All of the aforementioned components were supplied by Sigma-Aldrich, Merck, and MTI Corp. The received components were utilized throughout the whole work with no further removals.

2.2. Synthesis of p-g-C_3N_4 and CuO@p-g-C_3N_4. A ceramic crucible containing 5 g of melamine was heated at a 5°C/min rate in a furnace set to 550°C for 4 h. The resulting light yellow powder was labeled as bulk g-C_3N_4 and vigorously agitated for 10 h in a mixed solution of 50 mL of deionized water, 20 mL of HCl, and 20 mL of HNO_3 to create pores. Furthermore, p-g-C_3N_4 and copper chloride were mixed at a ratio of 1 : 0.2 wt% in 60 mL of deionized water and subjected to an ultrasonic treatment process for 1 h. The final

product is transferred to a 100 mL Teflon-lined stainless steel autoclave and heated to 180°C for 12 h. The resulting precipitate was washed five times with DI water and ethanol solutions. The precipitation was then dried overnight at 100°C in a hot air oven. The collected final products were preserved in the glass vials and properly sealed with the lid. Then, the lid was taped with Teflon and paraffin tape layers to avoid air contamination. Finally, these packed vials were kept in the vacuum desiccator to prevent the ingress of moisture. The resulting p-g-C_3N_4 and CuO@p-g-C_3N_4 samples were used to analyze their microstructural and electrochemical properties.

2.2.1. Microstructural Characteristics. The phase and crystallinity of the synthesized samples were determined by the X-ray diffraction (MPD for bulk, 3 kW, PANalytical with 1.5406 Å of Cu Kα radiation) technique. Morphology and elemental analyses were assessed using field emission scanning electron microscopy (FESEM, Hitachi S-4800) and transmission electron microscopy (TEM, Tecnai G2 F20ST Win) mounted to the EDS analyzer, respectively. The elemental composition of the sample was evaluated using X-ray photoelectron spectroscopy (Thermo Scientific using Al Kα radiation under the pressure of 5×10^{-9} Torr).

2.2.2. Electrochemical Characteristics

(1) Electrode Preparation. To make a working electrode, 80 wt% of the active sample, 10 wt% of PVDF, and 10 wt% of carbon black are mixed well and formed into a homogeneous slurry with the addition of a few drops of N-methyl-2-pyrrolidinone. The slurry was evenly dispersed throughout the nickel foam ($1 \times 1\ cm^2$ area), and the mass loadings of the p-g-C_3N_4 and CuO@p-g-C_3N_4 electrodes are 10 and 16 mg cm^{-2}, respectively. A platinum mesh (10×10 mm) and Ag/AgCl/3 M KCl (Ω Metrohm) are used as counter and reference electrodes.

The electrochemical properties (CV, GCD, and EIS) of the synthesized electrodes were investigated at room temperature using a CHI 760 E instrument in a 3 M KOH aqueous electrolyte. The specific capacitance of the synthesized electrodes was estimated using equations (1)–(3) based on the integral area of the cyclic voltammetry (CV) curves, discharge time, and integral area under the discharge curve in galvanostatic charging/discharging (GCD) [18, 21, 22].

$$\mathrm{Cs\ (F/g)} = \frac{\int I\,\mathrm{dV}}{2 * m * v * \Delta V}, \tag{1}$$

$$\mathrm{Cs\ (F/g)} = \frac{I_\mathrm{d}\Delta t}{V}, \tag{2}$$

$$\mathrm{Cs\ (F/g)} = \frac{2I_\mathrm{d}\int V\,\mathrm{dt}}{\Delta V^2}. \tag{3}$$

Herein, the parameters $\int I\mathrm{dV}$ (A.V), m (g), I_d (A/g), Δt (s), $\int V\mathrm{dt}$ (Vs), and ΔV (V) represent the integral area of the CV curve, the mass of the active electrode, current density, discharge time, integral area of the discharge curve, and potential window, respectively. We synthesized each product twice and validated the phase and elemental composition by preliminary XRD, SEM, and EDS characterizations. Furthermore, the electrochemical characteristics of the produced electrodes were investigated three times and provided consistent findings owing to minimal error values (±1~±5 F/g).

3. Result and Discussion

3.1. Microstructural Characteristics. Figure 1 shows the X-ray diffraction spectra of as-synthesized p-g-C_3N_4 and CuO@p-g-C_3N_4 powders. The X-ray diffraction spikes at 13.20° and 27.41° were ascribed to the (100) and (002) orientations of carbon nitride (g-C_3N_4 # 01-087-1526). The presence of a prominent (002) peak implies layer stacking in conjugated aromatic systems [23–25]. On the other hand, the lower intensity (100) peak suggests a stratified packing structure of tri-s-triazine units. Peaks at 32.42°, 35.33°, 38.58°, 48.57°, 53.24°, 58.17°, 61.33°, 66.16°, 67.83°, 72.33°, and 74.83° are ascribed to (110), (002), (111), (-202), (020), (202), (-113), (-311), (113), (311), and (004) orientations of the monoclinic CuO phase (#01-089-5895) with C2/c space group [26–28]. The presence of an X-ray diffraction (002) peak at 27.67° confirms the existence of a graphitic structure. Because of the relatively uniform distribution of CuO particles over porous g-C_3N_4 nanosheets, the high-intensity diffraction peaks of CuO particles dominate the intensity of the (001) peak (disappearance). Also, the presence of both phases without any deviations in peak positions confirms that CuO particles and g-C_3N_4 nanosheets are well mixed in the composite. The average crystallite size (d) of both powders was determined using Debye-Scherrer's formula [6, 29]:

$$d = \frac{0.9\,\lambda}{\beta_{2\theta}\cos\theta}, \tag{4}$$

where λ is the wavelength of Cu Kα, $\beta_{2\theta}$ is the full width at half maxima, and θ represents the diffraction angle (radian). The predominant peaks were used to compute the average crystallite sizes of p-g-C_3N_4 and CuO@p-g-C_3N_4 samples, which were 7.9 nm and 17.32 nm, respectively.

The morphological information of the produced p-g-C_3N_4 and CuO@p-g-C_3N_4 samples was captured by FESEM and is displayed in Figures 2(a)–2(d). All of the images depict a sheet-like morphology with a porous nature. In CuO@p-g-C_3N_4, because of the lower particle size and homogenous embedding of the CuO particles on the nanosheets, the presence of CuO particles in the composite is not clearly apparent. As a result, the surface morphology of the samples was clearly shown by TEM (Figures 3(a)–3(f)) examination.

The p-g-C_3N_4 and CuO@p-g-C_3N_4 samples have porous and sheet-like surfaces. Tiny CuO particles are implanted in the p-g-C_3N_4 nanosheets in the CuO@p-g-C_3N_4 composite. The presence of copper oxide nanoparticles on the porous g-C_3N_4 sheets increases the electroactive sites, enhancing electric conductivity and electrochemical performance. Figures 3(b) and 3(f) show high-resolution TEM images

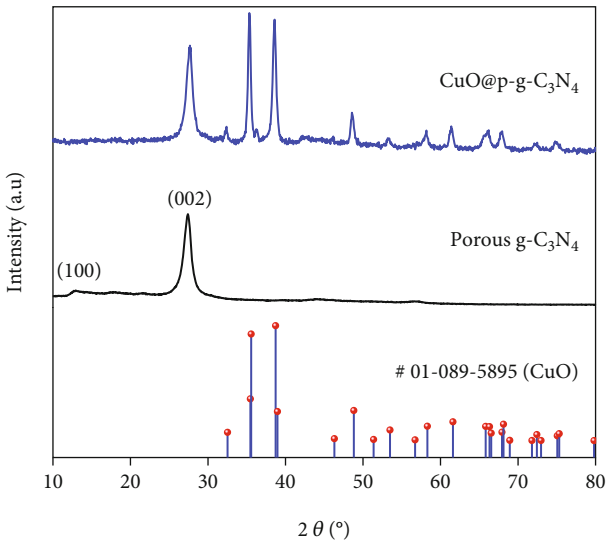

Figure 1: XRD spectra of porous g-C_3N_4 and CuO@p-g-C_3N_4 samples.

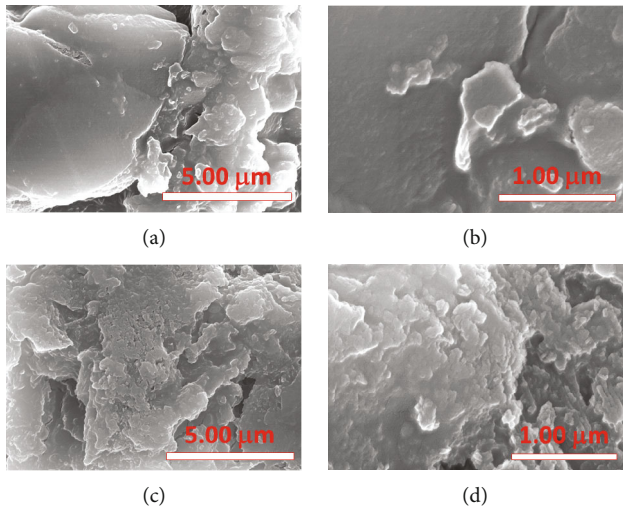

Figure 2: FESEM image of (a, b) p-g-C_3N_4 and (c, d) CuO@p-g-C_3N_4 samples at different magnifications.

of p-g-C_3N_4 nanosheets and copper oxide-decorated p-g-C_3N_4 nanosheets. The d-spacing between the bright fringes is 0.336 nm for the (002) planes of p-g-C_3N_4 (inset down: Figure 3(f)) and 0.232 nm for the (111) planes of the CuO phase (inset top: Figure 3(f)), respectively [30]. The SAED pattern of p-g-C_3N_4 (Figure 3(c)) shows diffused rings pertaining to the carbon nitride's (001) and (002) planes; however, the d-spacing values are slightly smaller than the standard data. In CuO@p-g-C_3N_4, bright spots with circular rings in the SAED pattern (inset Figure 3(e)) indicate the nanocrystalline structure corresponding to the (001), (100), (101), (002), and (102) planes.

Figures 4(a) and 4(b) illustrate the corresponding EDS spectra of p-g-C_3N_4 and CuO@p-g-C_3N_4 samples, with the analyzed area of the sample depicted in the inset figures, respectively. The exhibited peaks at 0.28 and 0.39 keV in the lower energy regions of the EDS spectrum ascribed to

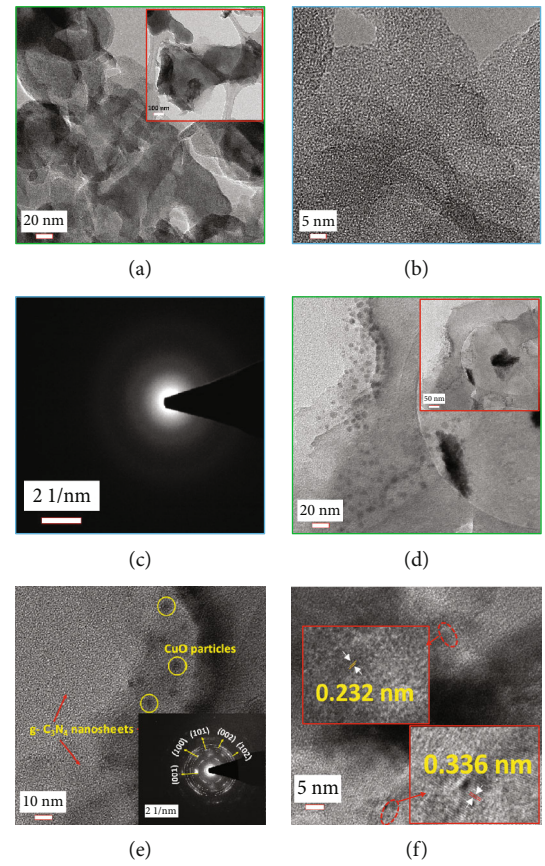

Figure 3: (a) TEM image (inset: TEM with 100 nm scale), (b) HR-TEM, and (c) SAED pattern of p-g-C_3N_4; (d) TEM image (inset: TEM with 50 nm scale), (e) TEM (inset: SAED pattern), and (f) HR-TEM (CuO (111) d-spacing, inset top; g-C_3N_4 (002) d-spacing, inset down) images of CuO@p-g-C_3N_4.

carbon (C) and nitrogen (N) elements, as well as two peaks around 8-9 keV, confirming the presence of the copper (Kα, Kβ) element from the grid source. Furthermore, additional peaks at 0.53 and 0.94 keV belong to the oxygen (Kα) and copper (Cu Lα) elements from the CuO@p-g-C_3N_4 sample. Also, the atomic percentage ratio of carbon to nitrogen in both samples is 3 : 4, confirming the C_3N_4 phase.

The pore size and specific surface area reveal the reversibility of the reaction as well as the synergistic impact of the porous C_3N_4 nanosheet loading with CuO nanoparticles. The pore size and specific surface area of the materials are determined using N_2 isothermal adsorption/desorption experiments, as illustrated in Figures 5(a) and 5(b). According to the IUPAC classification, both samples' adsorption/desorption isotherms are type IV, with the adsorption curves in the low-pressure region biased towards the Y-axis, indicating the presence of micropores, and stronger interactions with the curves in the medium-pressure region, signifying that sample buildup has produced pore channels in the mesoporous range. The hysteresis lines in the high-pressure region are all of the H3 types. This implies that the stacked pores (macropores) are of the slit kind, which is also consistent with the porous stacked nanosheets shown

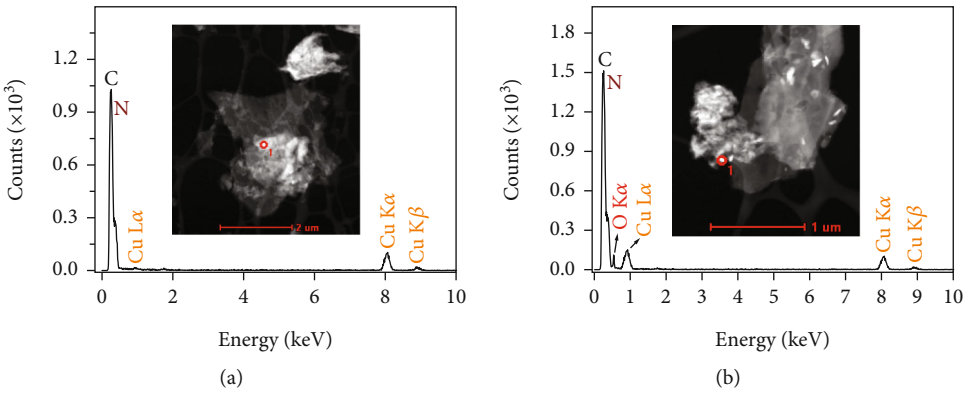

FIGURE 4: EDS spectra of (a) p-g-C_3N_4 and (b) CuO@p-g-C_3N_4 powder samples.

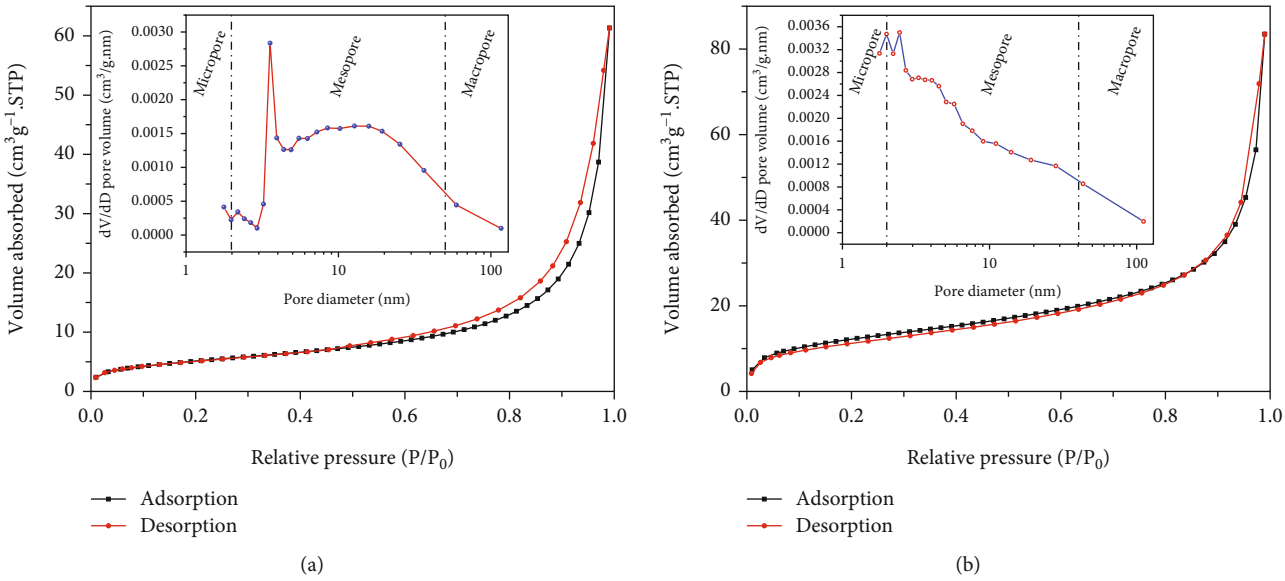

FIGURE 5: Nitrogen adsorption-desorption isotherms and corresponding pore size distribution curves (inset) of (a) p-g-C_3N_4 and (b) CuO@p-g-C_3N_4.

in the TEM images. The specific surface areas of p-g-C_3N_4 particles and CuO@p-g-C_3N_4 samples were 16.92 and 42.60 $m^2 g^{-1}$, respectively.

Pore size distribution graphs of p-g-C_3N_4 and CuO@p-g-C_3N_4 samples are presented in the inset of Figures 5(a) and 5(b). The pore size of the porous g-C_3N_4 sample was primarily between 1.77 nm and 116.8 nm, with an average pore size of 21.16 nm. The pore size of the CuO@p-g-C_3N_4 sample varied from 1.78 to 111.4 nm, with an average pore size of 15.98 nm. The CuO@p-g-C_3N_4 sample has a higher pore volume (0.1198 cm^3/g) than the porous g-C_3N_4 powder (0.0928 cm^3/g). The adsorption/desorption isotherms as well as the pore size distribution of the CuO@p-g-C_3N_4 sample make it abundantly evident that the attached CuO nanoparticles increase the number of micro- and mesopores between the stack layer of the porous carbon nitride nanosheets. This results in an increase in the sample's specific surface area and pore volume. This may improve the electroactive sites, which is good for electrochemical performance in terms of specific capacitance and stability.

The chemical structure of existing components on the surface of the CuO@p-g-C_3N_4sample was examined using XPS, as displayed in Figures 6(a)–6(d). The wide-scan survey spectrum (Figure 6(a)) of the CuO@p-g-C_3N_4 powder reveals the presence of C 1s, N 1s, O 1s, and Cu 2p elements in their binding energy ranges. The peak deconvolution in high-resolution XPS of C 1s (Figure 6(b)) consists of three peaks associated with binding energies of 287.5, 286.2, and 284.0 eV, corresponding to the C=N, C-O-C, and C-C bonds [31]. The N 1s spectrum deconvolution (Figure 6(c)) shows three peaks with binding energies of 400.3, 399.2, and 397.9 eV ascribed to the bridging nitrogen in N-$(C)_3$ (graphitic), C=N-C (pyrrolic), and =N-bonds (pyridine structures), respectively [32, 33]. The peak appeared at a binding energy of 530.8 eV assigned to the oxygen (O) 1s state. Furthermore, two predominant peaks with binding energies of 932 eV and 951 eV, as well as satellite peaks, correspond to Cu 2p1/2 and Cu 2p3/2. Each spin-orbit peak (Figure 6(d)) is deconvoluted into two peaks with binding energies of 931.8 and 951.6 eV and 933.3 and 953.1 eV,

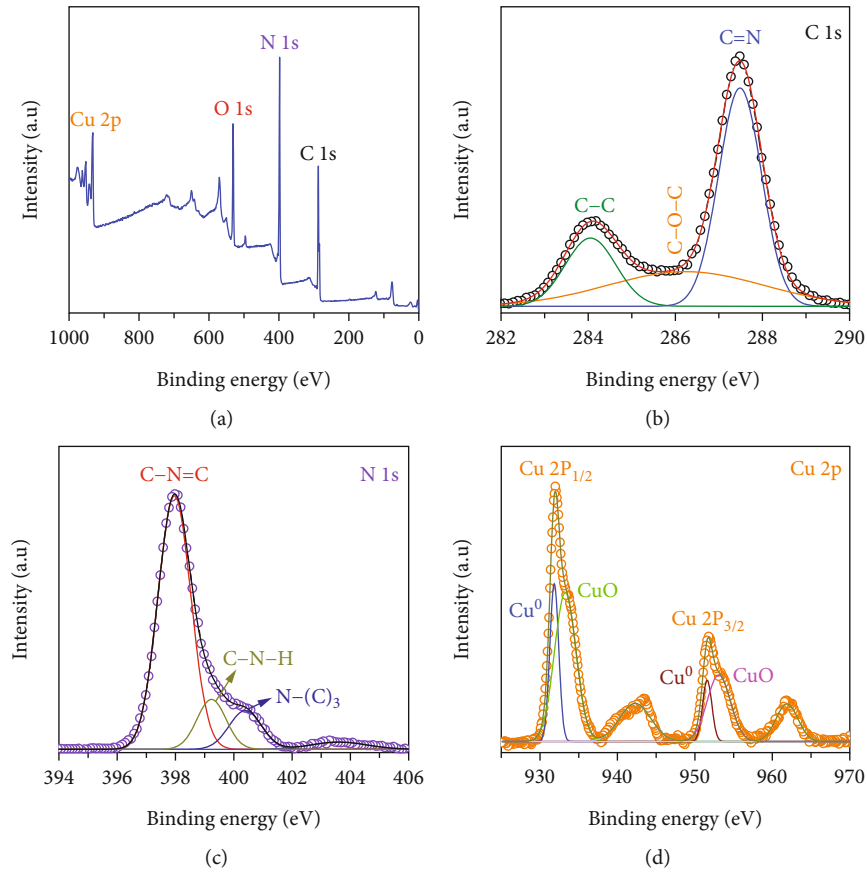

FIGURE 6: (a) XPS survey spectrum of CuO@p-g-C_3N_4 powder sample. High resolution of (b) C 1s, (c) N 1s, and (d) Cu 2p spin orbits.

corresponding to the metal Cu and CuO phases, respectively [34, 35]. The resolution spectra of the C 1s and N 1s peaks show the presence of g-C_3N_4 in the CuO@p-g-C_3N_4 sample.

3.2. Electrochemical Characteristics. In a 3 M KOH aqueous electrolyte solution, the electrochemical performance of p-g-C_3N_4 and CuO@p-g-C_3N_4 electrodes was investigated using a three-electrode cell and a CHI 706E electrochemical analyzer. Figure 7(a) shows the cyclic voltammetry curves of p-g-C_3N_4 and CuO@p-g-C_3N_4 electrodes at a scan rate of 10 mV/s. The broad oxidation and reduction peaks in CV curves, together with the constant $\Delta E_{a,c}$ (redox peak difference), indicate that the electrode material exhibits a pseudocapacitive behavior. The generated CV curves typically feature two separate regions: the area where the current depends on the potential (intercalation pseudocapacitance-type mechanism) and the area where the current does not depend on the potential (surface redox pseudocapacitance mechanism). Because of the existence of the CuO phase in the CuO@p-g-C_3N_4 electrode, the location of the oxidation and reduction peaks wiggles to a higher value, which is compatible with prior works of literature [36]. Besides that, the CuO@p-g-C_3N_4 sample has a larger integral area than the p-g-C_3N_4 sample, indicating that the CuO inclusion has an impact on the sample's current response. The calculated specific capacitance for both samples using CV curves is 28.76 and 88.07 F/g at a scan rate of 10 mV/s, respectively.

The current response of the p-g-C_3N_4 and CuO@p-g-C_3N_4 electrodes at different scan speeds (1-10 mV/s) over the working potential region of 0.0-0.45 V is shown in Figures 7(b) and 7(c)). As the scan rate was raised, the integrated region of the CV curves increased without altering their form, demonstrating high rate capability. According to the power law ($i_p = av^b$), the parameter "b" (slope) value from the logarithmic plot of peak current versus scan rate provides the kinetic information of the electrochemical reactions. Figure 7(d) shows the power law graphs of both samples, and the determined "b" values are 0.71/0.64 and 0.79/0.78 (oxidation/reduction peaks), which signifies pseudocapacitive storage kinetics (the larger contribution from capacitive controlled processes) [37].

In addition, the faradaic and capacitive current contributions of the CuO@p-g-C_3N_4 electrode at different scan rates were evaluated using the following expression, i.e., $I(V) = k_1 v + k_2 v^{1/2}$ where $I(V)$ and v are known values and k_1 and k_2 represent the slope and intercept values from the $I(V)/v^{1/2}$ versus $v^{1/2}$ graph at the corresponding applied scan rates [38]. The contribution of diffusion-controlled interaction (39.07%) and surface capacitance (60.93%) was found for the CuO@p-g-C_3N_4 electrode at a scan rate of 10 mV/s, as shown in Figure 7(e). The diffusion control and surface capacitive contributions were 66.97% and 33.03%, respectively, at a scan rate of 1 mV/s. Figure 7(f) demonstrates that the surface capacitive contribution increases and the

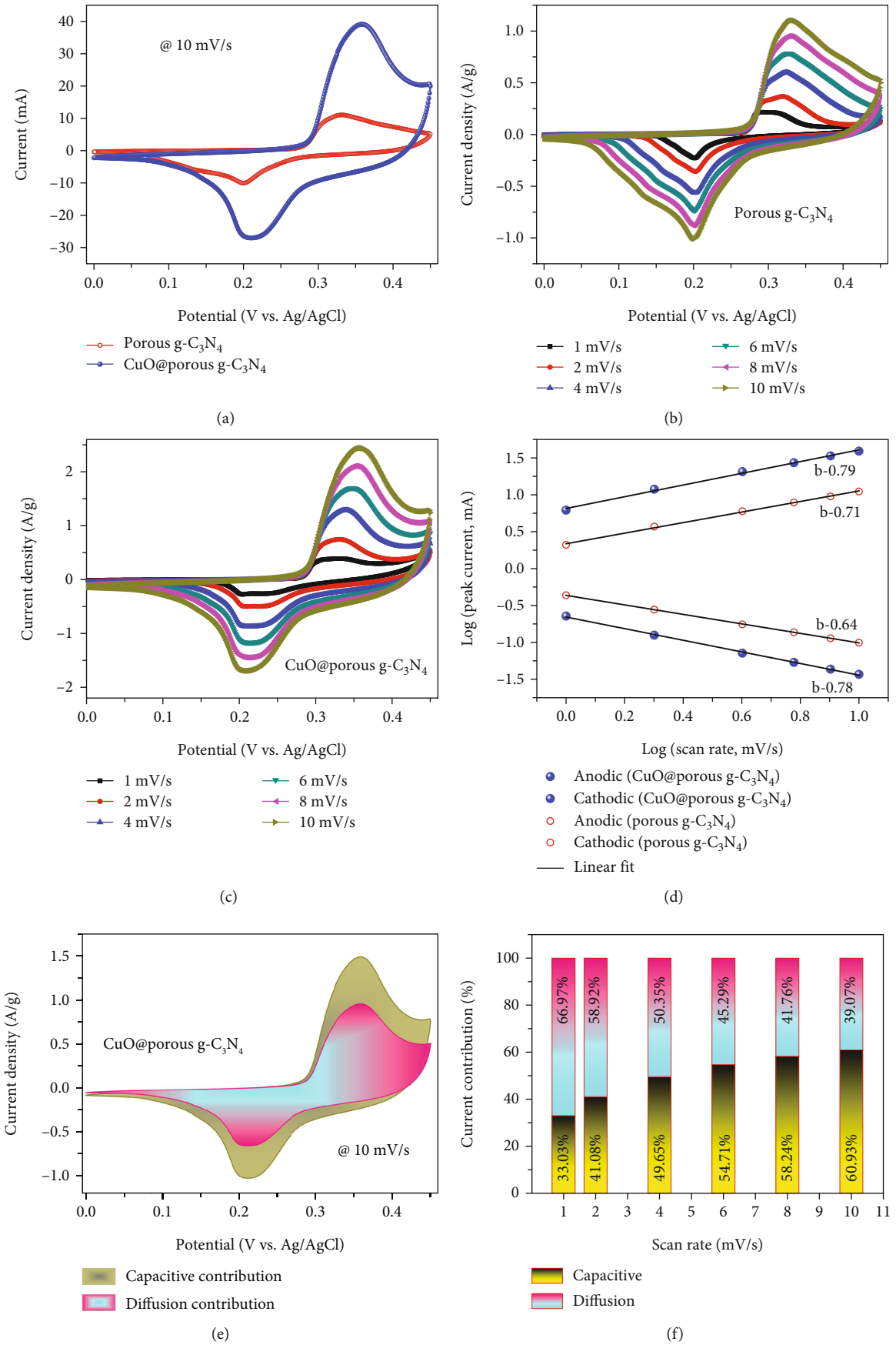

Figure 7: Continued.

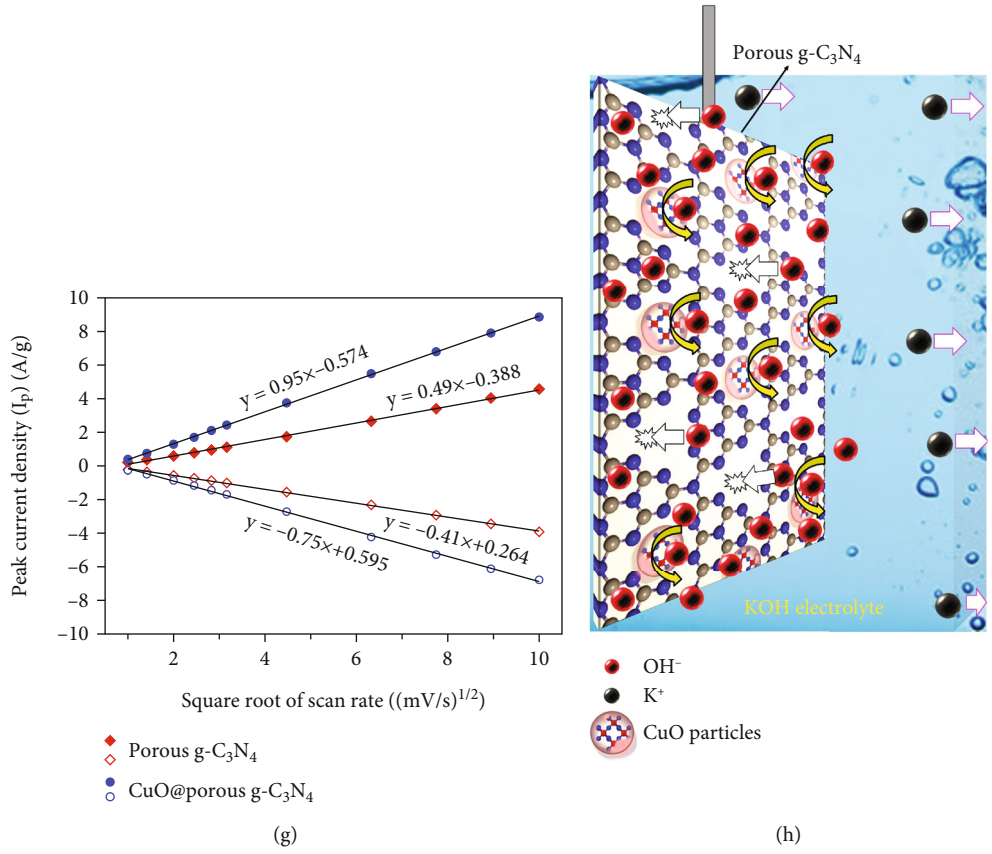

FIGURE 7: (a) CV curves of p-g-C_3N_4 and CuO@p-g-C_3N_4 electrodes at a scan rate of 10 mV/s. (b, c) CV curves of the p-g-C_3N_4 and CuO@p-g-C_3N_4 electrode at various scan rates (1-10 mV/s). (d) Log v versus log i_p graphs. (e) Square root of scan rate versus peak current density graphs of p-g-C_3N_4 and CuO@p-g-C_3N_4 electrodes. (f) Ratio of the current contribution at different sweep rates of the CuO@p-g-C_3N_4. (g) Pseudocapacitive contribution of the CuO@p-g-C_3N_4 electrode at 10 mV/s. (h) Schematic illustration of redox reactions at CuO@p-g-C_3N_4 electrode in three-electrode system.

diffusion-controlled contribution decreases with increasing scan rate. This is due to the shorter ion interaction time afforded by the electrode materials at higher scan rates. In addition, the adsorption of electroactive ions onto the surface or near-surface region of carbon nitride nanosheets dominates the faradaic reactions from the CuO nanoparticles due to the lower weight percentage of CuO in the composite (see Figure 7(h)). Therefore, a capacitive charge storage mechanism dominates the faradaic storage process by increasing the applied sweep voltage.

Furthermore, the addition of copper oxide particles to the porous g-C_3N_4 nanosheets increases the number of electroactive sites (diffusion centers). The electroactive sites in the faradaic behavior electrode are associated with the OH^- ion diffusion coefficient, which is evaluated using the Randles-Sevcik equation [39]:

$$I_p = \left(2.69 \times 10^5\right) \times n^{3/2} \times A \times \sqrt{D_{OH^-}} \times C_{OH^-} \times \sqrt{v}. \quad (5)$$

In this regard, the graph between the peak current and the square root of the scan rate of both electrodes is plotted and shown in Figure 7(g). The following is the ratio of diffusion coefficients in CuO@p-g-C_3N_4 and p-g-C_3N_4 electrodes:

$$\frac{D_{(\mathrm{CuO@p\text{-}g\text{-}C_3N_4})}}{D_{(\mathrm{p\text{-}g\text{-}C_3N_4})}} = \left[\frac{\left(I_P/v^{1/2}\right)_{(\mathrm{CuO@p\text{-}g\text{-}C_3N_4})}}{\left(I_P/v^{1/2}\right)_{(\mathrm{p\text{-}g\text{-}C_3N_4})}}\right]^2 = \left[\frac{0.95}{0.49}\right]^2 = 3.76, \quad (6)$$

$$D_{(\mathrm{CuO@p\text{-}g\text{-}C_3N_4})} = 3.76\, D_{(\mathrm{p\text{-}g\text{-}C_3N_4})}.$$

The diffusion coefficient estimated for the CuO@p-g-C_3N_4 electrode is 3.76 times greater than that of the p-g-C_3N_4 electrode. However, the measured specific capacitances of the p-g-C_3N_4 electrode were 36.80, 34.55, 33.11, 31.79, 30.33, and 28.76 F/g at a scan rate of 1, 2, 4, 6, 8, and 10 mV/s. In addition, the specific capacitances of the CuO@p-g-C_3N_4 electrode were 129.77, 121.06, 109.02, 98.96, 93.30, and 88.07 F/g for scan rates of 1, 2, 4, 6, 8, and 10 mV/s, respectively. It concludes that CuO@p-g-C_3N_4 has higher specific capacitance values than porous g-C_3N_4 electrodes at respective sweep rates. As a result, it is important to emphasize that CuO

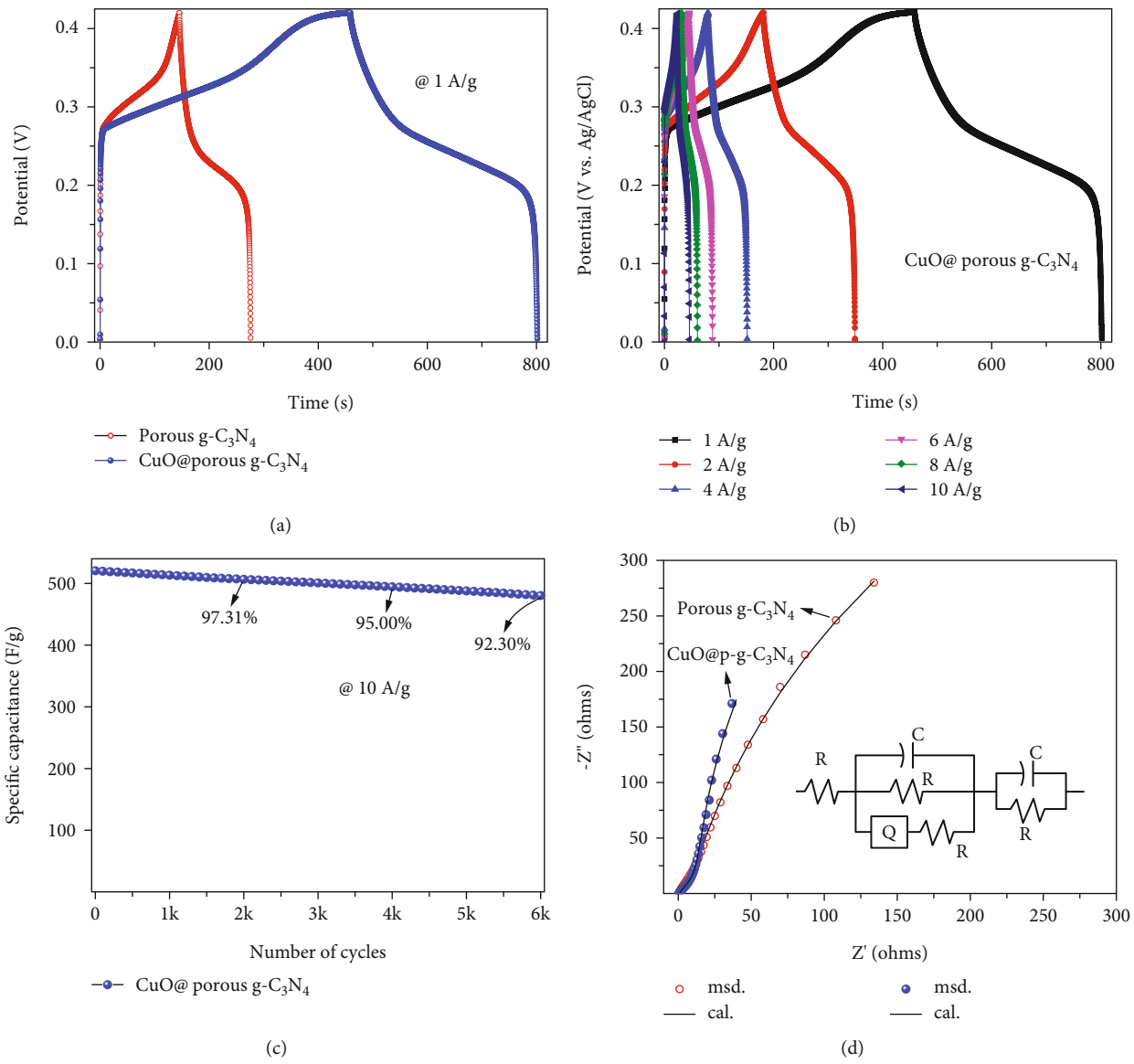

Figure 8: (a) GCD curves of p-g-C_3N_4 and CuO@p-g-C_3N_4 electrodes at a current density of 1 A g^{-1}. (b) GCD curves of CuO@ p-g-C_3N_4 electrode at different current densities (1-10 A g^{-1}). (c) Long cycling test for CuO@ p-g-C_3N_4 electrodes. (d) EIS spectra of p-g-C_3N_4 and CuO@ p-g-C_3N_4 electrodes.

nanoparticles anchored on porous g-C_3N_4 nanosheets promote more electroactive sites and increase charge transfer dynamics, enhancing the specific capacitance of the electrode. When the scan rate rises, the number of electrolyte ions accessible to the working electrode decreases, resulting in a decrease in specific capacitance at higher scan rates.

The electrochemical interaction between the KOH electrolyte and the prepared CuO@p-g-C_3N_4 electrode is schematically depicted in Figure 7(h) for clarity. Based on the present CV findings as well as prior experimental results, the charging and discharging processes in the CuO@p-g-C_3N_4 electrode in alkaline (KOH) electrolyte within a potential window of 0 to 0.45 V may be expressed as follows.

(i) When the voltage is scanned from 0 to 0.45 V, electrons are released from the electrode. This is because g-C_3N_4 interacts with hydroxide ions (OH^-) from the KOH electrolyte to create oxygen-functionalized g-C_3N_4 (g-C_3N_4-O), and the process can be represented as

$$gC_3N_4 + 2OH^- \longrightarrow gC_3N_4 - O + e^- + H_2O \quad (7)$$

During the reverse scan from 0.45 to 0.0 V, the oxygen-containing functional groups on the surface of g-C_3N_4 react with hydroxide ions (OH^-) and gain electrons (e^-) to regenerate g-C_3N_4 and produce water (H_2O).

$$gC_3N_4 - O + OH^- + e^- \longrightarrow gC_3N_4 + H_2O \quad (8)$$

(ii) Conversely, the redox peaks indicate that the attached CuO particles undergo faradaic (Cu^+/Cu^{2+}) redox processes. In the reduction process

Table 1: Comparison of the electrochemical performance of CuO@p-g-C_3N_4 electrodes with reported electrodes.

S. no.	Electrode	Electrolyte	Specific capacity or capacitance (C/g or F/g)	Current density (A/g)	Cycle stability	Ref.
1	ZM-C-800	6 M KOH	359.1	1	98.3% after 10,000 cycles at 1 A/g	[43]
2	S-gC_3N_4/CoS_2	3.5 M KOH	180 C/g	1	83% after 15,000 cycles at 50 A/g	[44]
3	PPy&C_3N_4 composite	0.1 M $LiClO_4$	810	0.2	92% after 6000 cycles at 6.0 A/g	[45]
4	CoO/GCN-NS	6 M KOH	458	0.5	—	[46]
5	CuO/GCN-NS	6 M KOH	154.5	0.5	—	[46]
6	g-C_3N_4 nanosheet @CoAl-LDH	2 M KOH	343.3	5	95.28% after 6000 cycles at 7.0 A/g	[47]
7	Boron-doped g-C_3N_4	1.0 M $2SO_4$	660.6	0.1	107.3% after 10,000 cycles at 10 A/g	[20]
8	Ag decorated PANI/g-C_3N_4	1 M H_2SO_4	797.8	1.0	84.43% after 1000 cycles at 1 A/g	[33]
9	g-C_3N_4/Co_3O_4	1 M KOH	201	1.0	97% after 6000 cycles at 5 A/g	[17]
10	TiS_2/g-C_3N_4	2 M KOH	165.9	1.0	87% after 2500 cycles	[18]
11	C/CuO@g-C_3N_4	0.5 M NaOH	247.2	1.0	92.1% after 6000 cycles at 1 A/g	[48]
12	CuO/g-C_3N_4	2 M KOH	384	2.0	98.02% after 5000 cycles at 10 A g^{-1}	[49]
13	Nanoporous gold/g-C_3N_4	0.5 M Na_2SO_4	440	2.0	98% after 10,000 cycles	[21]
14	$MnMoO_4$@g-C_3N_4/CNT	1 M NaCl	252.4	1.0	—	[50]
15	CuO/carbon nanosheets	1 M Na_2SO_4 1 M KOH	183.9 371.1	1.0	87% after 2000 cycles at 1 A/g 51.3% after 2000 cycles at 1 A/g	[51]
16	MOF-derived CuO/g-C_3N_4	2 M KOH	1530.4	2.0	66.3% after 3000 cycles at 10 A g^{-1}	[52]
17	GO/CuO	1 M Na_2SO_4	245	0.1	79% after 1000 cycles at 0.25 A g^{-1}	[53]
18	CuO@p-g-C_3N_4	3 M KOH	817	1.0	92.3% after 6000 cycles at 8 A g^{-1}	Present work

(0.45 to 0.0 V scan), CuO (and/or $Cu(OH)_2$) is converted into Cu_2O (and/or CuOH) by a gain of electrons in the cathode peak, while during the oxidation process (0.0 to 0.45 V scan), Cu_2O (and/or CuOH) is converted into CuO (and/or $Cu(OH)_2$) [40, 41]

$$\begin{aligned} \mathrm{CuO} + \frac{1}{2}\mathrm{H_2O} + \mathrm{e^-} &\leftrightarrow \frac{1}{2}\mathrm{Cu_2O} + \mathrm{OH^-} \\ \mathrm{Cu(OH)_2} + \mathrm{e^-} &\leftrightarrow \frac{1}{2}\mathrm{Cu_2O} + \frac{1}{2}\mathrm{H_2O} + \mathrm{OH^-} \\ \mathrm{CuOH} + \mathrm{OH^-} &\leftrightarrow \mathrm{CuO} + \mathrm{H_2O} + \mathrm{e^-} \\ \mathrm{CuOH} + \mathrm{OH^-} &\leftrightarrow \mathrm{Cu(OH)_2} + \mathrm{e^-} \end{aligned} \quad (9)$$

(iii) Another key feature is the porous nature of g-C_3N_4 nanosheets, which influences ion diffusion kinetics dependent on pore interconnectivity and effectively decreases electrode material resistance, affecting rate capability performance

Another trait known as galvanostatic charge-discharge can be used to calculate the specific capacitance of the electrodes. This is the temporal response when charging and discharging at various current densities (1–10 A g^{-1}) within the operating potential window of 0.0–0.42 V. Figure 8(a) demonstrates that the CuO@p-g-C_3N_4 electrode has a longer charge-discharge lifetime (at 1 A/g) than the p-g-C_3N_4 sample. Figure 8(b) illustrates the GCD curves of CuO@p-g-C_3N_4 electrodes at 1-10 A g^{-1}. During the charging process, the charges are accumulated on the surface from 0 to 0.27 V, and after that, charges are inserted/intercalated into the surface, resulting in a voltage plateau between 0.27 V and 0.42 V. During the discharge process, the potential decreases to a pseudoreversible plateau due to the transition from Cu^{2+} to Cu^+ along with deoxidizing of graphitic carbon nitride. The nonlinear GCD curves with voltage plateaus suggest that the pseudocapacitive mechanism occurred on the surface of the electrode material. The plateaus of the voltage in the GCD curves precisely match the CV curves. The projected discharge-specific capacitances of the p-g-C_3N_4 electrode were 311, 296, 273, 248, 224, and 194 F/g for 1, 2, 4, 6, 8, and 10 A/g, respectively. The calculated specific capacitances of CuO@p-g-C_3N_4 electrodes were 817, 795, 687, 608, 563, and 513 F/g for 1, 2, 4, 6, 8, and 10 A/g, respectively. Additionally, the determined specific capacitances of the p-g-C_3N_4 electrodes from the integral area under the discharge curve were 170.6, 159.2, 139.7, 123.1, 109.3, and 92.9 F g^{-1} at 1, 2, 4, 6, 8, and 10 A g^{-1}, respectively, while CuO@p-g-C_3N_4 electrodes delivered 496.6, 482.4, 407.0, 358.8, 325.2, and 297.6 F g^{-1} at 1, 2, 4, 6, 8, and 10 A g^{-1}, respectively.

Furthermore, the cycling performance of CuO@p-g-C_3N_4 electrodes was investigated by performing 6000 continuous cycles at a current density of 8 A/g, as shown in Figure 8(c). The electrode retained 97.31% of its capacitance

after 2000 cycles, 95.00% after 4000 cycles, and 92.30% after 6000 cycles, exhibiting exceptional cycling stability. It is concluded that the specific capacitance of the electrode (capacitance retention, 7.7%) was slightly decreased with testing time. In addition to redox reactions, which cause irreversible chemical processes that degrade the composition, the redox (faradaic) reactions of electrolyte ions during charge-discharge cycles to balance the total charge put mechanical stress on the electrode material's structure. The repetitive charge-discharge cycles surely generate mechanical and electrical defects that reduce initial performance due to active ingredient mass loss. The interfacial charge transfer between the electrolyte and electrode (p-g-C_3N_4 and CuO@p-g-C_3N_4) was identified using EIS analysis, and the Nyquist plot is shown in Figure 8(d). In the higher frequency zone, insertion of the impedance line with the real axis offers information about the ohmic resistance (Rs). The Rs values of p-g-C_3N_4 and CuO@p-g-C_3N_4 electrodes were 0.83 and 0.63 Ω, respectively. The electrode's low ohmic resistance shows low contact and solution resistance, indicating the electrochemical cell's strong conductivity. The absence of a semicircle in the EIS at high frequencies is due to the parallel combination of the resistive and capacitive components, as well as low-frequency spikes with an upward slope. The R(CR(QR))(CR) analog circuit (inset figure) had chi-square values of 2.79×10^{-2} and 2.93×10^{-2}, respectively, that matched the measured impedance lines. The electrical equivalent circuit R(CR(QR))(CR) model is composed of the electrolyte and pore resistance (R_s), the adsorption capacitance and resistance (C_a and R_a), a constant phase element (Q) used to compensate for the roughness of the electrode and used as a model for the double-layer capacitor (C_{dl}) and inhomogeneity in the system, the charge transfer resistance (R_{ct}), and the resistance and capacitance of the electrode (R_e and C_e). R_a and C_a are associated with the charging/discharging processes that occur at the surface of the electrode [42]. Indeed, when compared to previously reported electrodes, the electrochemical performance (Table 1) of the CuO@ porous g-C_3N_4 electrode demonstrated the highest specific capacitance. The synergistic effect between porous g-C_3N_4 and CuO nanoparticles provides specific capacitance, lower charge transfer resistance, and good cycling stability of the CuO@p-g-C_3N_4 electrode.

4. Conclusions

In summary, copper oxide particles anchored on the porous g-C_3N_4 sample were synthesized by using the sequential heating-acidic-hydrothermal treatment process. First, thermal heating was employed on the melamine to create a graphitic carbon nitride at 550°C. Second, the acidic treatment was applied to the g-C_3N_4 to make it porous in the sample. Finally, copper oxide particles were uniformly anchored on the surface of the porous g-C_3N_4 using hydrothermal synthesis. The X-ray diffraction peaks confirm the existence of both g-C_3N_4 and CuO phases without any impurities. The morphological features of the samples and elemental composition confirm the porous structure of the graphitic carbon nitride phase. The anchored CuO nanoparticles reduce the stacking of graphitic carbon nitride nanosheets and also enhance 2.5 times of specific surface area than porous g-C_3N_4. In the composite electrode, the surface-controlled pseudocapacitive mechanism was observed from the g-C_3N_4 nanosheets, in which the surface of nanosheets reacted with OH^- ions and oxidized/deoxidized. CuO nanoparticles exhibit faradaic behavior through Cu^+/Cu^{2+} transitions during the redox reactions. The synergistic effect of both materials in the composite increases the electroactive sites leading to the integral area from the CV curve, and the time taken for charge/discharging reactions was higher than the porous g-C_3N_4. The electrical conductivity and ionic transit channel are both enhanced by the synergistic impact of creating porous structures and uniformly dispersing copper oxide particles. However, the CuO@p-g-C_3N_4 electrode demonstrated 817 F g^{-1} at 1 A g^{-1} of specific capacitance and admirable capacitance retention (92.3% after 6000 cycles). It is possible that the suggested simulated strategy would encourage the creation of high-performance CuO@p-g-C_3N_4 composite electrodes with controlled porosity architectures for use in supercapacitors and other energy gadgets.

Data Availability

The authors can also make data available on request through a data access committee, institutional review board, or the authors themselves.

Conflicts of Interest

The authors declare no competing financial interests.

Authors' Contributions

Dhananjaya Merum contributed in the conceptualization and investigation and wrote the original draft. Rosaiah Pitcheri wrote, reviewed, and edited the manuscript. Nipa Roy assisted in the preparation and data acquisition. K Naveen Kumar participated in the methodology and investigation. Ammar Mohamed Tighezza contributed in data acquisition and formal analysis. Soumyendu Roy wrote, reviewed, and edited the manuscript. Sang Woo Joo carried out project administration, supervision, and editing.

Acknowledgments

(1) This work is supported by NRF-2019R1A5A8080290 of the National Research Foundation of Korea. The authors thank the Core Research Support Center for Natural Products and Medical Materials (CRCNM) for technical support regarding the micro-Raman spectrophotometer analyses. (2) The work was supported by Researchers Supporting Project number RSPD2024R765, King Saud University, Riyadh, Saudi Arabia.

Supplementary Materials

Graphical abstract. *(Supplementary Materials)*

References

[1] S. Chen, Y. Wang, H. Du, and Z. Cui, "The current situation, development aims and policy recommendation of China's electric power industry," *International Journal of Climate Change Strategies and Management*, vol. 15, no. 2, pp. 282–299, 2023.

[2] M. A. Hannan, S. M. Abu, A. Q. Al-Shetwi et al., "Hydrogen energy storage integrated battery and supercapacitor based hybrid power system: a statistical analysis towards future research directions," *International Journal of Hydrogen Energy*, vol. 47, no. 93, pp. 39523–39548, 2022.

[3] S. Biswas and A. Chowdhury, "Organic supercapacitors as the next generation energy storage device: emergence, opportunity, and challenges," *ChemPhysChem*, vol. 24, no. 3, pp. 1–18, 2023.

[4] B. M. Al-Maswari, N. Al-Zaqri, K. Alkanad et al., "Magnesium bismuth ferrite nitrogen-doped carbon nanomagnetic perovskite: synthesis and characterization as a high-performance electrode in a supercapacitor for energy storage," *ACS Omega*, vol. 8, no. 18, pp. 16145–16157, 2023.

[5] M. Z. Ullah Shah, H. Hou, M. Sajjad, M. S. Shah, K. Safeen, and A. Shah, "Iron-selenide-based titanium dioxide nanocomposites as a novel electrode material for asymmetric supercapacitors operating at 2.3 V," *Nanoscale Advances*, vol. 5, no. 5, pp. 1465–1477, 2023.

[6] D. Merum, L. N. Ambadi, H. O. Mahammad et al., "Direct growth of cobalt-doped nickel vanadate shelf-like architectures on Ni foam electrodes for solid-state alkaline battery," *Journal of Alloys and Compounds*, vol. 950, article 169771, 2023.

[7] N. Dhiman, V. Sharma, and S. Ghosh, "Perspective on biomass-based cotton-derived nanocarbon for multifunctional energy storage and harvesting applications," *ACS Applied Electronic Materials*, vol. 5, no. 4, pp. 1970–1991, 2023.

[8] M. Du and K. Zhang, "Nanoporous conducting polymer nanowire network-encapsulated MnO_2-based flexible supercapacitor with enhanced rate capability and cycling stability," *ACS Applied Materials & Interfaces*, vol. 15, no. 18, pp. 22563–22573, 2023.

[9] J. Zhang, X. Wang, G. Hang et al., "Recent advances in MXene-based fibers, yarns, and fabrics for wearable energy storage devices applications," *ACS Applied Electronic Materials*, vol. 5, no. 9, pp. 4704–4725, 2023.

[10] C. Chen, N. W. Li, B. Wang, S. Yuan, and L. Yu, "Advanced pillared designs for two-dimensional materials in electrochemical energy storage," *Nanoscale Advances*, vol. 2, no. 12, pp. 5496–5503, 2020.

[11] Y. Yang, X. Liu, Z. Zhu et al., "The role of geometric sites in 2D materials for energy storage," *Joule*, vol. 2, no. 6, pp. 1075–1094, 2018.

[12] H. Y. Xu, L. C. Wu, H. Zhao, L. G. Jin, and S. Y. Qi, "Synergic effect between adsorption and photocatalysis of metal-free g-C3N4 derived from different precursors," *PLoS One*, vol. 10, no. 11, pp. 1–20, 2015.

[13] J. Fang, H. Fan, Z. Zhu, L. B. Kong, and L. Ma, ""Dyed" graphitic carbon nitride with greatly extended visible-light-responsive range for hydrogen evolution," *Journal of Catalysis*, vol. 339, pp. 93–101, 2016.

[14] F. Dong, Y. Li, Z. Wang, and W. K. Ho, "Enhanced visible light photocatalytic activity and oxidation ability of porous graphene-like g-C3N4 nanosheets via thermal exfoliation," *Applied Surface Science*, vol. 358, pp. 393–403, 2015.

[15] T. Aditya, J. Jana, A. Pal, and T. Pal, "One-pot fabrication of perforated graphitic carbon nitride nanosheets decorated with copper oxide by controlled ammonia and sulfur trioxide release for enhanced catalytic activity," *ACS Omega*, vol. 3, no. 8, pp. 9318–9332, 2018.

[16] J. Ma, X. Y. Tao, S. X. Zhou et al., "Facile fabrication of Ag/PANI/g-C_3N_4 composite with enhanced electrochemical performance as supercapacitor electrode," *Journal of Electroanalytical Chemistry*, vol. 835, pp. 346–353, 2019.

[17] J. Kavil, P. M. Anjana, D. Joshy et al., "g-C_3N_4/CuO and g-C_3N_4/Co_3O_4 nanohybrid structures as efficient electrode materials in symmetric supercapacitors," *RSC Advances*, vol. 9, no. 66, pp. 38430–38437, 2019.

[18] G. Nabi, K. N. Riaz, M. Nazir et al., "Cogent synergic effect of TiS_2/g-C_3N_4 composite with enhanced electrochemical performance for supercapacitor," *Ceramics International*, vol. 46, no. 17, pp. 27601–27607, 2020.

[19] V. Ragupathi, P. Panigrahi, and N. G. Subramaniam, "g-C_3N_4 doped MnS as high performance electrode material for supercapacitor application," *Materials Letters*, vol. 246, pp. 88–91, 2019.

[20] L. Kong, Q. Chen, X. Shen, G. Zhu, and J. Zhu, "Ionic liquid directed construction of foam-like mesoporous boron-doped graphitic carbon nitride electrode for high-performance supercapacitor," *Journal of Colloid and Interface Science*, vol. 532, pp. 261–271, 2018.

[21] A. Y. Chen, T. T. Zhang, Y. J. Qiu et al., "Construction of nanoporous gold/g-C_3N_4 heterostructure for electrochemical supercapacitor," *Electrochimica Acta*, vol. 294, pp. 260–267, 2019.

[22] P. Xu, K. Ye, D. Cao et al., "Facile synthesis of cobalt manganese oxides nanowires on nickel foam with superior electrochemical performance," *Journal of Power Sources*, vol. 268, pp. 204–211, 2014.

[23] Z. Yang, L. Li, H. Yu et al., "Facile synthesis of highly crystalline g-C_3N_4 nanosheets with remarkable visible light photocatalytic activity for antibiotics removal," *Chemosphere*, vol. 271, article 129503, 2021.

[24] H. Azizi-Toupkanloo, M. Karimi-Nazarabad, M. Shakeri, and M. Eftekhari, "Photocatalytic mineralization of hard-degradable morphine by visible light-driven Ag@g-C_3N_4 nanostructures," *Environmental Science and Pollution Research*, vol. 26, no. 30, pp. 30941–30953, 2019.

[25] M. Q. Wen, T. Xiong, Z. G. Zang, W. Wei, X. S. Tang, and F. Dong, "Synthesis of MoS_2/g-C_3N_4 nanocomposites with enhanced visible-light photocatalytic activity for the removal of nitric oxide (NO)," *Optics Express*, vol. 24, no. 10, pp. 10205–10212, 2016.

[26] K. Rajendran, J. Yadav, T. S. Khan, M. A. Haider, S. Gupta, and D. Jagadeesan, "Oxygen vacancy-mediated reactivity: the curious case of reduction of nitroquinoline to aminoquinoline by CuO," *Journal of Physical Chemistry C*, vol. 127, no. 18, pp. 8576–8584, 2023.

[27] D. Limthin, P. Leepheng, B. Tunhoo et al., "Preparation of surface-modified electrode of copper(ii) oxide mixed with the molecularly imprinted polymer for enhancement of melamine detection with photoelectrochemical technique," *RSC Advances*, vol. 13, no. 21, pp. 14729–14736, 2023.

[28] S. Kumar, N. Bhawna, A. Gupta et al., "New insights into Cu/Cu_2O/CuO nanocomposite heterojunction facilitating

photocatalytic generation of green fuel and detoxification of organic pollutants," *The Journal of Physical Chemistry C*, vol. 127, no. 15, pp. 7095–7106, 2023.

[29] D. Merum, R. Pitcheri, V. Gonuguntla, and S. W. Joo, "Synthesis and properties of oxygen-deficient cobalt oxide nanocubes for supercapacitor application," *Materials Letters*, vol. 347, article 134585, 2023.

[30] B. Abebe, D. Tsegaye, C. Sori, R. C. Renuka Prasad, and H. A. Murthy, "Cu/CuO-doped ZnO nanocomposites via solution combustion synthesis for catalytic 4-nitrophenol reduction," *ACS Omega*, vol. 8, no. 10, pp. 9597–9606, 2023.

[31] J. R. Zhang, Y. Ma, S. Y. Wang et al., "Accurate K-edge X-ray photoelectron and absorption spectra of g-C_3N_4 nanosheets by first-principles simulations and reinterpretations," *Physical Chemistry Chemical Physics*, vol. 21, no. 41, pp. 22819–22830, 2019.

[32] G. Feng, H. Huang, M. Zhang et al., "Single atom iron-doped graphic-phase C_3N_4 semiconductor nanosheets for augmented sonodynamic melanoma therapy synergy with endowed chemodynamic effect," *Advancement of Science*, vol. 10, no. 23, pp. 1–14, 2023.

[33] J. S. Ma, H. Yang, S. Kubendhiran, and L. Y. Lin, "Novel synthesis of sulfur-doped graphitic carbon nitride and $NiCo_2S_4$ composites as efficient active materials for supercapacitors," *Journal of Alloys and Compounds*, vol. 903, article 163972, 2022.

[34] H. N. Abdelhamid and G. A. E. Mahmoud, "Antifungal and nanozyme activities of metal–organic framework-derived CuO@ C," *Applied Organometallic Chemistry*, vol. 37, no. 3, pp. 1–10, 2023.

[35] M. Jamal, M. M. Billah, and S. A. Ayon, "Opto-structural and magnetic properties of fluorine doped CuO nanoparticles: an experimental study," *Ceramics International*, vol. 49, no. 6, pp. 10107–10118, 2023.

[36] S. Zhou, W. Wei, Y. Zhang, S. Cui, W. Chen, and L. Mi, "Heterojunction α-$Co(OH)_2$/α-$Ni(OH)_2$ nanorods arrays on Ni foam with high utilization rate and excellent structure stability for high-performance supercapacitor," *Scientific Reports*, vol. 9, no. 1, pp. 1–12, 2019.

[37] S. W. J. Dhananjaya Merum, R. R. Nallapureddy, M. R. Pallavolu et al., "Pseudocapacitive performance of freestanding Ni3V2O8Nanosheets for high energy and power density asymmetric supercapacitors," *ACS Applied Energy Materials*, vol. 5, no. 5, pp. 5561–5578, 2022.

[38] D. Merum, N. Parvin, S. V. P. Vattikuti et al., "Impact of Co-doping on the microstructural and electrochemical features of mesoporous 3D oval–shaped $Ni_{3-x}Co_xV_2O_8$ electrodes for high-performance hybrid supercapacitors," *Journal of Energy Storage*, vol. 61, article 106674, 2023.

[39] Z. Abdi, M. Vandichel, A. S. Sologubenko et al., "The importance of identifying the true catalyst when using Randles-Sevcik equation to calculate turnover frequency," *International Journal of Hydrogen Energy*, vol. 46, no. 76, pp. 37774–37781, 2021.

[40] M. R. Pallavolu, A. N. Banerjee, and S. W. Joo, "Battery-type behavior of Al-doped CuO nanoflakes to fabricate a high-performance hybrid supercapacitor device for superior energy storage applications," *Coatings*, vol. 13, no. 8, p. 1337, 2023.

[41] V. Senthilkumar, Y. S. Kim, S. Chandrasekaran, B. Rajagopalan, E. J. Kim, and J. S. Chung, "Comparative supercapacitance performance of CuO nanostructures for energy storage device applications," *RSC Advances*, vol. 5, no. 26, pp. 20545–20553, 2015.

[42] T. Karazehir, M. Ates, and A. S. Sarac, "Mott-Schottky and morphologic analysis of poly(pyrrole-N-propionic acid) in various electrolyte systems," *International Journal of Electrochemical Science*, vol. 10, no. 8, pp. 6146–6163, 2015.

[43] C. Cai, Y. Zou, C. Xiang et al., "Broccoli-like porous carbon nitride from ZIF-8 and melamine for high performance supercapacitors," *Applied Surface Science*, vol. 440, pp. 47–54, 2018.

[44] S. Vinoth, K. Subramani, W. J. Ong, M. Sathish, and A. Pandikumar, "CoS_2 engulfed ultra-thin S-doped g-C_3N_4 and its enhanced electrochemical performance in hybrid asymmetric supercapacitor," *Journal of Colloid and Interface Science*, vol. 584, pp. 204–215, 2021.

[45] R. Gonçalves, R. S. Paiva, T. M. Lima, M. W. Paixão, and E. C. Pereira, "Carbon nitride/polypyrrole composite supercapacitor: boosting performance and stability," *Electrochimica Acta*, vol. 368, article 137570, 2021.

[46] R. S. Santos, R. Suresh Babu, M. Devendiran, D. B. Haddad, and A. L. F. de Barros, "Facile synthesis of transition metal (M=Cu, Co) oxide grafted graphitic carbon nitride nanosheets for high performance asymmetric supercapacitors," *Materials Letters*, vol. 308, article 131156, 2022.

[47] S. Sanati and Z. Rezvani, "g-C_3N_4 nanosheet@CoAl-layered double hydroxide composites for electrochemical energy storage in supercapacitors," *Chemical Engineering Journal*, vol. 362, pp. 743–757, 2019.

[48] S. V. P. Vattikuti, B. P. Reddy, C. Byon, and J. Shim, "Carbon/CuO nanosphere-anchored g-C_3N_4 nanosheets as ternary electrode material for supercapacitors," *Journal of Solid State Chemistry*, vol. 262, pp. 106–111, 2018.

[49] K. G. Subhash, M. D. Benoy, J. Duraimurugan, R. Siranjeevi, and S. Prabhu, "Synthesis, and characterization of CuO/g-C_3N_4 nanocomposites for high performances supercapacitor application," *Materials Letters*, vol. 330, article 133288, 2023.

[50] V. M. Rangaraj, J. Yoo, J. Song, and V. Mittal, "Three-dimensional (3D) $MnMoO_4$@ g-C_3N_4/CNT hybrid composite electrode for hybrid capacitive deionization," *Separation and Purification Technology*, vol. 317, article 123898, 2023.

[51] X. Yuan, X. Yan, C. Zhou et al., "Decorating carbon nanosheets with copper oxide nanoparticles for boosting the electrochemical performance of symmetric coin cell supercapacitor with different electrolytes," *Ceramics International*, vol. 46, no. 1, pp. 435–443, 2020.

[52] Z. Zhu, C. Wei, D. Jiang, X. Wu, and M. Lu, "Design and synthesis of MOF-derived CuO/g-C_3N_4 composites with octahedral structures as advanced anode materials for asymmetric supercapacitors with high energy and power densities," *Materials Advances*, vol. 3, no. 1, pp. 672–681, 2022.

[53] A. Pendashteh, M. F. Mousavi, and M. S. Rahmanifar, "Fabrication of anchored copper oxide nanoparticles on graphene oxide nanosheets via an electrostatic coprecipitation and its application as supercapacitor," *Electrochimica Acta*, vol. 88, pp. 347–357, 2013.